Atmospheric
Measurement
Techniques
Open Access

Discussions

Cloud speed sensor

V. Fung, J. L. Bosch, S. W. Roberts, and J. Kleissl

Department of Mechanical and Aerospace Engineering, University of California, San Diego, California, USA

Correspondence to: J. Kleissl (jkleissl@ucsd.edu)

AMTD

6, 9037–9059, 2013

Cloud speed sensor

V. Fung et al.

Abstract

Changing cloud cover is a major source of solar radiation variability and poses challenges for the integration of solar energy. A compact and economical system that measures cloud motion vectors to estimate power plant ramp rates and provide short term
5 solar irradiance forecasts is presented. The Cloud Speed Sensor (CSS) is constructed using an array of luminance sensors and high-speed data acquisition to resolve the progression of cloud passages across the sensor footprint. An embedded microcontroller acquires the sensor data and uses a cross-correlation algorithm to determine cloud motion vectors. The CSS was validated against an artificial shading test appara-
10 tus, an alternative method of cloud motion detection from ground measured irradiance (Linear Cloud Edge, LCE), and a UC San Diego Sky Imager (USI). The CSS detected artificial shadow directions and speeds to within 15 and 6 % accuracy, respectively. The CSS detected (real) cloud directions and speeds without average bias and with average weighted root mean square difference of 22° and 1.9 m s^{-1} when compared to USI
15 and 33° and 1.5 m s^{-1} when compared to LCE results.

1   Introduction

Given the impact of fossil fuel consumption on the environment it is imperative that renewable energy provide a greater fraction of world energy demand. On average, the earth receives 8000 times more solar energy than the energy consumed globally, mak-
20 ing solar energy a strong candidate for supplying future world energy needs. However, difficulties in integrating variable generators into the electric grid have impacted the rate of large scale adoption of solar power. The variability of the solar resource could be better accommodated by grid operators if fluctuations in irradiance caused by cloud cover could be predicted.
25   Understanding cloud motion is critical for ramp rate estimation and short-term forecasting (Castro et al., 2013; Coimbra et al., 2013; Lave et al., 2012, 2013b), because

Title Page

Abstract | Introduction

Conclusions | References

Tables | Figures

◄ | ►

Back | Close

Full Screen / Esc

Printer-friendly Version

Interactive Discussion

cloud motion causes a sudden shortage or oversupply in solar power and must be compensated with an opposing ramp of energy storage or conventional generation. Previous studies have used satellite imagery for estimating cloud motion (Leese et al., 1971; Hammer et al., 1999; Lorenz et al., 2004; Perez et al., 2010). However, due to satel-
5   lite navigation, resolution, and parallax uncertainties, such cloud motion estimates are of limited use in very short-term, intra-hour forecasting. Other methods are based on ground measurements. For example, Hinkelman et al. (2011) determined cloud speeds by analyzing the time lag in maximum cross-correlation between two sensors aligned with the cloud direction, but the method cannot be automated since cloud direction has
10   to be known a priori. Weigl et al. (2012) derived velocity vectors from spatial irradiation data by considering rectangular clouds and tracking the movement of irradiation minima across the sensor array. Recently, two different approaches to determine cloud motion vectors were developed and validated by Bosch et al. (2013) using ground-based solar radiation measurements. The first approach (further developed in Bosch
15   and Kleissl, 2013) considers the dynamic equations of a linear cloud edge (LCE) that does not require orthogonality to the cloud motion passing through a sensor triplet and will be used in this paper for validation. The second method is based on the most correlated pair (MCP) of sensors arranged in 12 m diameter semi-circular array and lays the foundation of the cloud speed sensor (CSS) described here. However, the limited
20   sampling frequency requires sensor spacings of 10 s of meters and does not permit these methods to detect cloud speeds with enough resolution to cover the full range of naturally occurring cloud speeds. Also, the systems are not self-contained and cannot perform post-analysis of the acquired data. A smaller, self-contained, and much faster sampling version of the semicircle system is required for commercial use and
25   described in this paper.

Section 2 describes the theoretical concept for the Cloud Motion Vector (CMV) measurement similar to the previous semicircle sensor in Bosch et al. (2013). Sections 3.1 and 3.2 focus on the phototransistor characteristics, housing, and layout. In Sect. 3.3 the data acquisition and post-processing system is presented and quality con-

trol is discussed. Performance parameters and limitations of the CSS are mentioned in Sect. 3.4. Validation procedures for the algorithm and cloud motion results are described in Sects. 3.5 and 3.6. Section 3.7 describes the deployment and demonstration of the CSS at the UC San Diego Solar Energy test bed. Section 4 presents the results from field testing against USI and LCE results.

2 Theory: Most Correlated Pair method (MCP)

Variability of solar irradiance at the Earth's surface is mostly due to clouds shadows with varying light intensity. We describe a system to obtain cloud motion vectors using an array of ground-based sensors to measure the spatio-temporal variation of solar irradiance over the extent of the sensor array. Using the MCP method described in Bosch et al. (2013), the largest similarity in a pair of signals indicates alignment with the direction of cloud motion and is determined by the cross-correlation coefficient $R_{ab}(\Delta t)$:

$$R_{ab}(\Delta t) = \frac{1}{n} \sum_{m=1}^{n} \left(\frac{L_{a,t}(m) - \overline{L}_{a,t}}{\hat{L}_{a,t}} \right) \left(\frac{L_{b,t+\Delta t}(m) - \overline{L}_{b,t+\Delta t}}{\hat{L}_{b,t+\Delta t}} \right) \tag{1}$$

where a and b are sensor indices, n is the number of sample points, t and $t + \Delta t$ correspond to the time and lagged time, L_a and L_b are solar irradiance time series, overbars indicate averages and hats indicate standard deviations.

Assuming sensors S_a and S_b are the pair with largest R_{ab}, the detected solar irradiance signals will be similar, but will be delayed by a time lag, $\Delta t = t_{ab}$, as seen in Fig. 1.

Determining the time lag via cross correlation, the cloud speed can be found by

$$V_{\text{cloud}} = \frac{D}{t_{ab}} \tag{2}$$

where D is the distance separating the sensors.

3 Cloud speed sensor (CSS)

The CSS (Fig. 2) design objectives are compactness, fast data acquisition rates, robustness, and on-board processing. The implementation includes a high-performance microcontroller platform with built-in data acquisition and storage capability, and an array of phototransistors. The following subsections describe the system in more detail.

3.1 Luminance sensors

Solar radiation sensors consist of an array of nine phototransistors (TEPT4400, Vishay Intertechnology, Inc., USA). The sensors have a spectral response ranging from approximately 350 to 1000 nm with a peak response at 570 nm. The manufacturer has characterized the sensors over an operating temperature range of −40 to +90 °C. Response time was determined experimentally in our laboratory and found to be 21 µs rise time (10–90 % response). Excitation voltage for the sensors was 3.3 VDC supplied from a voltage regulator (LM2937-3.3, Texas Instruments, Inc., USA) and applied to the phototransistor collector (Fig. 3). A 2 kΩ load resistor was connected from the sensor emitter to system ground. The sensor outputs were taken at the emitter-load resistor junction and fed to analog input channels on the microcontroller.

In addition to the true mathematics mentioned above, there are a number of pseudo-mathematical theories, but these cannot be seriously considered by reputable scientists.

3.2 Sensor array

CMVs were determined with the phototransistors configured as an array of eight sensors positioned about a central sensor on a circle of radius 0.297 m, covering 0–105° in 15° increments (Figs. 2 and 4). Cross-correlation coefficients were computed for each pair of sensors (central sensor and a sensor on the circle) to determine cloud speed and direction based on Eqs. (1)–(2).

Title Page

Abstract | Introduction

Conclusions | References

Tables | Figures

◄ | ►

◄ | ►

Back | Close

Full Screen / Esc

Printer-friendly Version

Interactive Discussion

Each sensor was placed at the base of and inside a black opaque tube of diameter 6.35 mm and height 14.3 mm. The tube dimensions were designed to accommodate the 30° field of view of the TEPT4400 sensor. Fitted into the top of the tube was a section of translucent acrylic to act as a light diffuser/collector. When tested under halogen lights the diffuser was determined to have no effect on the incident light spectrum within the spectral response range of the sensor.

3.3 Data acquisition and post-processing

The microcontroller-based data acquisition system and sensors are powered from a small rechargeable 12 VDC sealed lead-acid battery. Regulated voltages (5 VDC for the microcontroller, 3.3 VDC for the sensors) are derived from the battery using integrated circuit voltage regulators (Fig. 3). We configured the data acquisition system using a high-performance 32 MIPS, 32-bit microcontroller platform (chipKIT Max32, Digilent Inc., USA) running at 80 MHz. The on-board static memory allows fast storage of up to 6000 10-bit data points per sensor. With our sampling rate of 667 samples s^{-1}, 6000 data points can be acquired and stored in approximately nine seconds. Then the data array is transferred to an off-board microSD card in four seconds, for archiving and further analysis.

Alternatively, on-board post-processing is available and the results can then be relayed to a central computer through serial or wireless communication. The cloud speed and direction are computed using an algorithm based on Eq. (1) in the Arduino Environment. Computing the largest cross-correlation for every time step (i.e. $m = 1$ to 5600 in 400 steps) would require 18 min. Optimization reduced the processing time to approximately 2 min. First, assuming a monotonous "smooth" signal, the cross-correlation time shift is performed in increments of 10 time steps instead of the standard of one time step. Then, the temporary maximum cross correlation is located and the surrounding 10 cross correlations are computed in time steps of one to determine the exact t_{ab} for the maximum cross correlation. Second, $\overline{L}_b$ and $\hat{L}_b$ of each cross correlation are

updated based on the previous $\overline{L}_b$ and $\hat{L}_b$. Through extensive post-processing analysis this algorithm has proven to be robust in finding t_{ab}.

Quality control during post-analysis is required to increase the robustness of the algorithm (Bosch et al., 2013). Most importantly, periods of small variability in the signal (for example during clear conditions) or small correlation coefficients are excluded. In specific, the range in a set of measurements must exceed 7 % of the maximum (clear day at solar noon) illuminance and there must be a maximum cross correlation R_{ab} greater than 0.95. Both treshold values were detemined through an extensive iterative process. These thresholds ensure that a cloud passage occurred which results in large signal to noise and is more likely to produce correct CMVs. In addition, measurements with several identical maximum cross correlations across different sensor pairs or unphysical cloud speeds (greater than $50\,\mathrm{m\,s^{-1}}$ is very unlikely) are discarded. Lastly, a moving median filter is computed at every timestep to determine the central tendency of quality controlled results within the past 30 min. While there is a potential to delay the detection of a change in cloud motion, CMVs generally change over longer time scales.

Calibration is also necessary since the TEPT4400s are not factory calibrated and vary in sensitivity. Miscalibration would result in a false t_{ab} because in the absence of peaks the cross correlation cannot determine if two signals are separated in time or signal magnitude. Calibrating each outer sensor with respect to the central sensor in 15 min intervals using linear regression mitigates this source of error.

3.4 Performance parameters and limitations

Based on typical cloud speeds obtained over the US (Bosch and Kleissl, 2013; Lave et al., 2013a), the CSS was designed to detect cloud speeds of up to $15\,\mathrm{m\,s^{-1}}$ with at least $1\,\mathrm{m\,s^{-1}}$ resolution. The maximum resolution of detectable cloud speeds is determined by the radius of the semicircle ($D = 0.297$ m, Eq. 2) and the sampling time step ($\Delta t = 0.0015$ s). For the CSS design, the resolvable cloud speeds are given by $\frac{D}{N\Delta t}$,

where $N = 1, \ldots, k$. k defines the maximum number of time shifts used in the cross-correlation computations. In this case we select the minimum cloud speed as $1\,\mathrm{m\,s^{-1}}$, which yields $k = 200$. Cloud speeds of less than $1\,\mathrm{m\,s^{-1}}$ are unusual and have little relevance to solar power as the resulting ramp rates would be slow and approach the cloud lifetime (Jiang et al., 2006). With 6000 samples in each array, the central 5600 values are shifted in the cross correlation, leaving $k = 200$ bidirectional time shifts to determine time lag. The direction of the shift that produces the maximum cross correlation indicates whether the clouds are moving in one direction or the opposite. The largest and smallest resolvable cloud speeds are therefore $\frac{D}{\Delta t} = \frac{0.297\,\mathrm{m}}{0.0015\,\mathrm{s}} = 198.1\,\mathrm{m\,s^{-1}}$ and $\frac{D}{k\Delta t} = \frac{0.297\,\mathrm{m}}{200 \times 0.0015\,\mathrm{s}} = 0.99\,\mathrm{m\,s^{-1}}$, respectively. The cloud speed resolution scales with $\frac{1}{N}$ such that very large cloud speeds are obtained at poor resolution (for example the second largest speed is $\frac{0.297\,\mathrm{m}}{2 \times 0.0005\,\mathrm{s}} = 99.1\,\mathrm{m\,s^{-1}}$) while smaller cloud speeds can be detected at higher resolution.

3.5 Validation using artificial shadows

Prior to measuring complex ground radiation patterns caused by clouds, a performance test with a simple shadow of known relative velocity was used to validate the CSS. Under clear conditions at solar noon, a stationary shadow was created from a suspended object. The CSS was mounted on a mobile platform that was pulled at a constant speed by a torque motor. Relative velocity vectors between the shadow and sensor can be determined by the motor rotational speed and orientation of the sensor. The magnitude of the irradiance reduction (i.e. the signal for Eq. 1) in the shadow decreases with increasing height of the object because of increased diffuse irradiance. Consequently, the CSS was first tested with a dark shadow from an object positioned 0.23 m above the CSS. The CSS was moved at a known CSS speed of $0.51\,\mathrm{m\,s^{-1}}$ with different directions (60 and 90°). Since the known CSS velocities do not fall within the range of detectable cloud speeds (see Sect. 3.4), $k = 600$ was used to reduce the smallest resolvable cloud speed to $0.33\,\mathrm{m\,s^{-1}}$ for this experiment. The procedure was repeated

with the object raised to 1.35 m above the CSS to observe how the influence of increased diffuse irradiance affects the measurements post-processing, and CMVs.

For all conditions, the detected directions were correctly identified and the detected shadow speed fell within 6 % of the true speed (Table 1), which is acceptable for CSS application. Only for experiment number 2, the detected direction was off by 15°, but the maximum correlation coefficients for the 90 and 105° directions were essentially indistinguishable with a difference of 0.0006. These results validate the basic concept, realization, and algorithm of the CSS to measure cloud speed and direction.

3.6 Deployment and validation against two cloud motion sensors

The CSS was deployed on nine days over a period of five months from March to August 2013 at the UC San Diego Solar Energy test bed in La Jolla, CA (Table 2). For validation, a sky imager was deployed adjacent to the CSS and a consistent coordinate system was established. The UCSD Sky Imager (USI, Chow et al., 2011; Urquhart et al., 2013; Yang et al., 2013), captures images using an upward-facing charge-coupled device (CCD) image sensor sensing RGB channels at 12 bit precision and 1748 × 1748 pixel resolution. A 4.5 mm circular fisheye lens allows imaging the entire sky hemisphere. Utilizing composite high dynamic range (HDR) imaging, the USI outputs images at 16 bit with a dynamic range of 84 dB. The images used in this analysis were taken by a rooftop-mounted USI located at 32.8722° N, 117.2410° W, and 129 m m.s.l. capturing images every 30 s. A cross-correlation method is applied to derive a representative cloud vector for the image (Yang et al., 2013).

USI cloud directions are expected to be accurate, but cloud speeds scale linearly with cloud height which is difficult to determine. Therefore the LCE approach (see introduction and Bosch et al., 2013; Bosch and Kleissl, 2013) was applied to three photodiode pyranometers (Li-200SZ, Licor, Inc.). The pyranometers were co-located on the USI rooftop and setup in an orthogonal coordinate system with average separation of 7 m and logged to a single CR1000 (Campbell Scientific Inc.) datalogger with an acquisition frequency of 20 Hz.

4   Results and discussion

The predominant cloud conditions in coastal southern California are overcast stratocumulus and few to scattered cumulus. Table 2 shows the average cloud directions and speeds on the nine deployment days. Table 3 presents the corresponding root mean square difference (RMSD) and mean bias (MB).

The 23 July and 8 August deployments are selected for discussion in greater detail. The KNKX METAR station 9 km to the east reported the following conditions: The air temperature during the 23 July and 8 August deployments was 22–26 °C and 24–25 °C, respectively. Surface winds were 260° to 310° at 4.1 to 5.7 m s^{-1} for the 23 July deployment and 250 to 280° at 3.6 to 4.6 m s^{-1} on 8 August. There were few clouds at 400 m below scattered clouds at 900 to 1200 m a.g.l. on 23 July and few clouds at 460 m a.g.l. on 8 August.

The calibrated TEPT 4400 sensor readings and resultant CMVs for 23 July and 8 August are shown in Figs. 5 and 6. For 23 July, 20 % of the 1611 raw results satisfy the quality control criteria described in Sect. 3.3; most results are excluded since the variability did not exceed 7 % of full range as for example after 1400 PST. Sky imagery reveals that CMV results occurred in scattered stratocumulus cloud cover during 1200–1400 PST that became overcast after 1400 PST (differences to the METAR cloud observations can be explained by large spatial heterogeneity of cloud cover in this coastal area). Overcast conditions cause insufficient solar variability to pass the quality control criteria. However, the 30 min median filter causes CMV to persist into the overcast period such as during 1400–1430 PST. The CSS quality controlled directions indicate cloud movement from the West–Northwest (300°) direction, consistent with surface winds and visual inspection of sky imagery. USI and LCE data show an average cloud motion direction of 286 and 275° with RMSD of 14 and 35°, respectively. The CSS cloud speed ranges from 3 to 6.0 m s^{-1}. USI and LCE yield an average cloud speed of 3.9 and 5.3 m s^{-1} with a RMSD of 1.2 and 1.2 m s^{-1} compared to CSS results, respectively.

On 8 August, visual inspection from sky imagery shows thin scattered stratocumulus clouds during 1030–1445 PST from WNW that became more widespread during 1445–1630 PST. Overcast conditions occurred after 1630 PST, which causes low solar irradiance variability and again produces no results. The CSS detects cloud movement from the WNW (299°) direction while USI and LCE detect average cloud directions of 286 and 283°, respectively. RMSD comparing CSS to USI and LCE direction results are 26 and 33°, respectively. The CSS cloud speed increases from 2 to $6.8\,\mathrm{m\,s^{-1}}$ during the deployment, which is consistent with the ranges and trends obtained by USI and LCE with RMSD of 0.9 and $1.3\,\mathrm{m\,s^{-1}}$, respectively. It is worth noting that all speeds results are similar during the period of high solar variability (1445–1600 PST) indicating more robustness during favorable cloud conditions. Although the three methods slightly differ in both detected direction and speed, the results lie within the range of CSS, USI, and LCE method uncertainty. True cloud speeds are not available and it is therefore unclear which sensor is more accurate.

Through extensive analysis presented in Tables 2 and 3, the CSS proves to be consistent with USI and LCE results for a wide range of cloud directions (southeasterly to northwesterly). The range of cloud speeds is more limited due to the low cloud heights and benign weather conditions in coastal southern California, but results are again consistent with the other methods. Overall speed and direction biases are essentially zero and typical RMSDs are $2\,\mathrm{m\,s^{-1}}$ and 30°.

5 Conclusions

Nine phototransistors arranged in a semicircular formation were used to obtain cloud motion vectors by finding the maximum signal cross-correlation between different pairs of sensors. Fast sampling rates by the microprocessor allowed the system to be compact, yet able to detect the full range of typical cloud speeds from 1 to $15\,\mathrm{m\,s^{-1}}$ (with $1\,\mathrm{m\,s^{-1}}$ resolution) and up to 24 with $2\,\mathrm{m\,s^{-1}}$ resolution. The CSS was validated using an artificial shading apparatus and found to detect cloud directions and speeds to within

15° and 6 % accuracy, respectively. Nine deployments on partly cloudy days resulted in consistent cloud directions and speeds with those observed from a sky imager and computed from the LCE method.

Unlike the prior proof of feasibility in Bosch et al. (2013), the present CSS system is self-contained and more economical while still producing accurate cloud motion vectors. With the present quality control criteria the CSS does not provide CMV results under uniform overcast conditions, but the small solar irradiance variability in overcast conditions does not present a major issue for solar power integration. Further optimization of the algorithm will refine quality control procedures to retain as many points as possible while ensuring robustness of the results.

References

Arias-Castro, E., Kleissl, J., Lave, M., Schweinsberg, J., and Williams, R.: A Poisson model for anisotropic solar ramp rate correlations, Sol. Energy, accepted, 2013.

Bosch, J. L. and Kleissl, J.: Cloud motion vectors fro a network of ground sensors in a solar power plant, Sol. Energy, 95, 13–20, 2013.

Bosch, J. L., Zheng, Y., and Kleissl, J.: Cloud velocity estimation from an array of solar radiation measurements, Sol. Energy, 87, 196–203, doi:10.1016/j.solener.2012.10.020, 2013.

Chow, C. W., Urquhart, B., Kleissl, J., Lave, M., Dominguez, A., Shields, J., and Washom, B.: Intra-hour forecasting with a total sky imager at the UC San Diego solar energy testbed, Sol. Energy, doi:10.1016/j.solener.2011.08.025, 2011.

Coimbra, C., Kleissl, J., and Marquez, R.: Overview of solar forecasting methods and a metric for accuracy evaluation, in: Solar Resource Assessment and Forecasting, edited by: Kleissl, J., Elsevier, Waltham, Massachusetts, 2013.

Hammer, A., Heinemann, D., Lorenz, E., and Lückehe, B.: Short-term forecasting of solar radiation: a statistical approach using satellite data, Sol. Energy, 67, 139–150, 1999.

Hinkelman, L., George, R., Wilcox, S., and Sengupta, M.: Spatial and temporal variability of incoming solar irradiance at a measurement site in Hawai'i, in: 91st American Meteorological Society Annual Meeting, 23–27 January 2011, Seattle, WA, United States, 2011.

Jiang, H., Xue, H., Teller, A., Feingold, G., and Levin, Z.: Aerosol effects on the lifetime of shallow cumulus, Geophys. Res. Lett., 33, L14806, doi:10.1029/2006GL026024, 2006.

Lave, M. and Kleissl, J.: Cloud speed impact on solar variability scaling – application to the wavelet variability model, Sol. Energy, 91, 11–21, doi:10.1016/j.solener.2013.01.023, 2013.

Lave, M., Kleissl, J., and Stein, J.: A Wavelet-based Variability Model (WVM) for solar PV powerplants, IEEE Transactions on Sustainable Energy, 99, doi:10.1109/TSTE.2012.2205716, 2012.

Lave, M., Stein, J., and Kleissl, J.: Quantifying and simulating solar power plant variability using irradiance data, in: Solar Resource Assessment and Forecasting, edited by: Kleissl, J., Elsevier, Waltham, Massachusetts, 2013.

Leese, J. A., Novak, C. S., and Clark, B. B.: An automated technique for obtaining cloud motion from geosynchronous satellite data using cross correlation, J. Appl. Meteorol., 10, 118–132, 1971.

Lorenz, E., Hammer, A., and Heinemann, D.: Short term forecasting of solar radiation based on satellite data, in: Proceedings of the ISES Europe Solar Congress EUROSUN2004, Freiburg, Germany, 20–24 June, 2004.

Perez, R., Kivalov, S., Schlemmer, J., Hemker Jr., K., Renné, D., and Hoff, T. E.: Validation of short and medium term operational solar radiation forecasts in the US, Sol. Energy, 84, 2161–2172, 2010.

Urquhart, B., Ghonima, M., Nguyen, D., Kurtz, B., Chow, C. W., and Kleissl, J.: Sky imaging systems for short-term forecasting, in: Solar Forecasting and Resource Assessment, edited by: Kleissl, J., Elsevier, Waltham, Massachusetts, 2013.

Weigl, T., Nagl, L., Weizenbeck, J., Zehner, M., Augel, M., Öchsner, P., Giesler, B., Becker, G., Mayer, O., Betts, T., and Gottschalg, R.: Modelling and validation of spatial irradiance characteristics for localised irradiance fluctuations and enhancements, in: 27th European Photovoltaic Solar Energy Conference, 24–28 September, Frankfurt, Germany, 3801–3804, 2012.

Title Page

Abstract | Introduction

Conclusions | References

Tables | Figures

◄ | ►

◄ | ►

Back | Close

Full Screen / Esc

Printer-friendly Version

Interactive Discussion

Yang, H., Chow, C. W., Ghonima, M., Kurtz, B., Nguyen, D., Urquhart, B., and Kleissl, J.: Solar irradiance forecasting using a ground-based sky imager developed at UC San Diego, Sol. Energy, submitted, 2013.

Cloud speed sensor

V. Fung et al.

Title Page

Abstract | Introduction

Conclusions | References

Tables | Figures

◄◄ | ►►

◄ | ►

Back | Close

Full Screen / Esc

Table 1. CSS performance for the artificial cloud shadow experiment.

Height of Object above CSS	True direction [°]	CSS direction [°]	True speed [m s^{-1}]	CSS speed [m s^{-1}]
0.23 m	60	60	0.51	0.48
0.23 m	90	105	0.51	0.48
1.35 m	60	60	0.51	0.48
1.35 m	270	270	0.51	0.48

Table 2. Deployment dates and average direction and speed for each cloud motion sensor. USI CMVs are unavailable for 14 March and 10 May due to incorrect cloud heights. LCE results are removed on 23 April due to an insufficient amount of results that passed quality control.

Date in 2013	Deployment [PST] All Methods	Average Direction [°]			Average Speed [m s^{-1}]		
		CSS	LCE	USI	CSS	LCE	USI
14 Mar	1030–1615	310	300	–	4.9	5.8	–
16 Mar	1415–1800	243	230	252	4.4	3.6	5.3
23 Apr	1000–1700	136	–	149	3.3	–	3.2
10 May	1345–1745	294	265	–	4.4	4.7	–
14 May	1010–1810	281	264	279	5.2	4.7	5.1
3 Jun	1250–1850	160	175	182	5.7	5.8	3.4
23 Jul	1200–1800	300	275	286	4.8	5.3	3.9
7 Aug	1135–1735	301	319	299	4.5	5.5	4.6
8 Aug	1030–1730	299	283	286	5.2	4.7	4.3

Table 3. RMSD and MB of CSS results compared to LCE and USI. Due to incorrect cloud height observed, no cloud motion results were detected from USI on 14 March and 10 May. LCE results are excluded for 23 April due to a shortage of results that pass quality control.

	RMSD				MB			
	Direction [°]		Speed [m s^{-1}]		Direction [°]		Speed [m s^{-1}]	
Date in 2013	LCE	USI	LCE	USI	LCE	USI	LCE	USI
14 Mar	41	–	3.0	–	8	–	−0.7	–
16 Mar	25	24	0.9	1.3	−8	−8	0.9	−0.9
23 Apr	–	20	–	0.6	–	−13	–	0.1
10 May	38	–	1.5	–	31	–	−0.6	–
14 May	24	20	0.9	2.5	13	1	0.4	−0.4
3 Jun	20	26	0.6	2.4	−15	−22	−0.2	2.2
23 Jul	35	14	1.2	1.2	25	14	−0.4	0.9
7 Aug	41	7	1.4	2.1	−18	2	−1.0	−0.2
8 Aug	37	26	1.3	0.9	13	13	0.4	−0.2
All	33	22	1.5	1.9	9	−0.7	−0.1	0.2
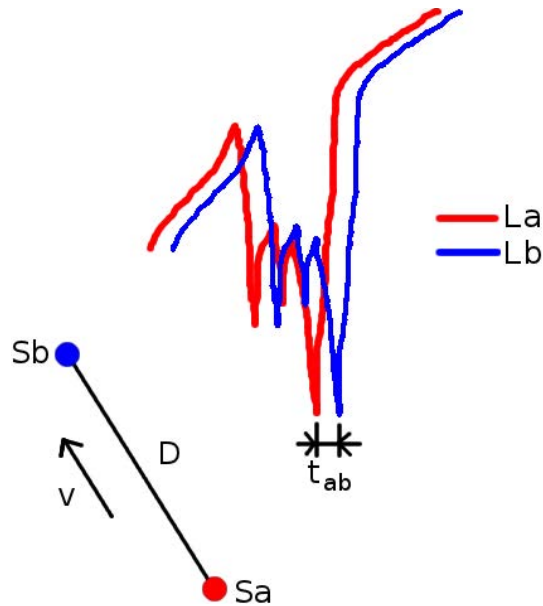
Fig. 1. Idealized sketch showing the most correlated pair of signals shifted by t_{ab} (adapted from Bosch et al., 2013).

Full Screen / Esc

Fig. 2. Cloud speed sensor (CSS). The entire system is contained inside a weather proof enclosure. On the top of the enclosure is the array of nine phototransistors used to measure the variation in solar radiation as clouds pass overhead.
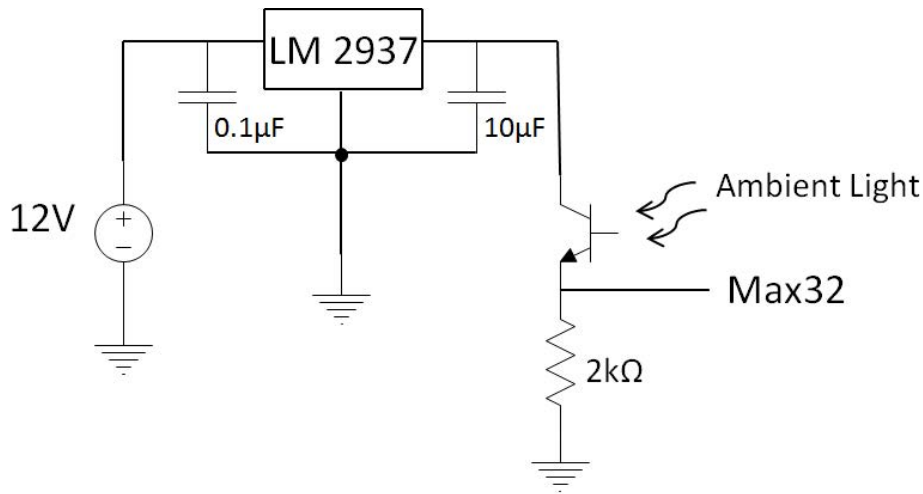
Fig. 3. Simplified schematic showing excitation voltage applied to the phototransistor collector, the 2 kΩ load resistor, and the sensor output as applied to an analog input channel on the microcontroller.
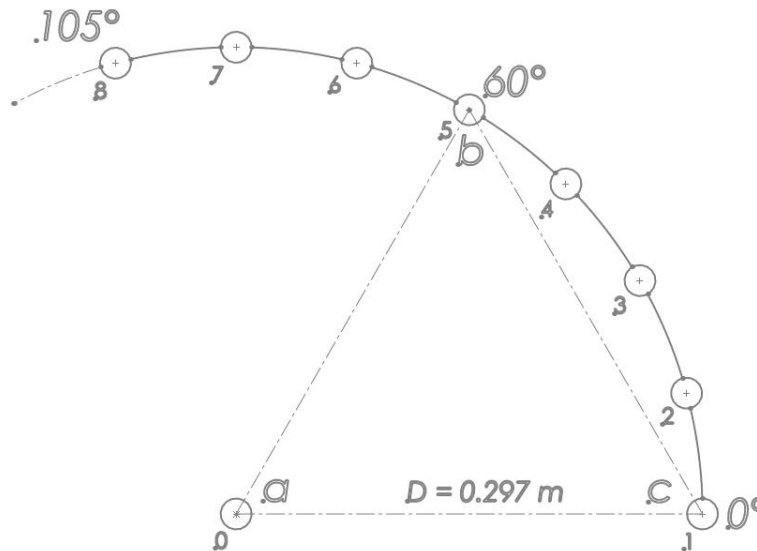
Fig. 4. Sensor arrangement. Each circle represents a sensor arranged in a circular pattern with a 15° spacing about the central sensor. Additional angles from 120° to 165° are obtained through equilateral triangles constructed from existing sensor positions. For example, for triangle *abc* the line from b to c results in an angle of 120°.
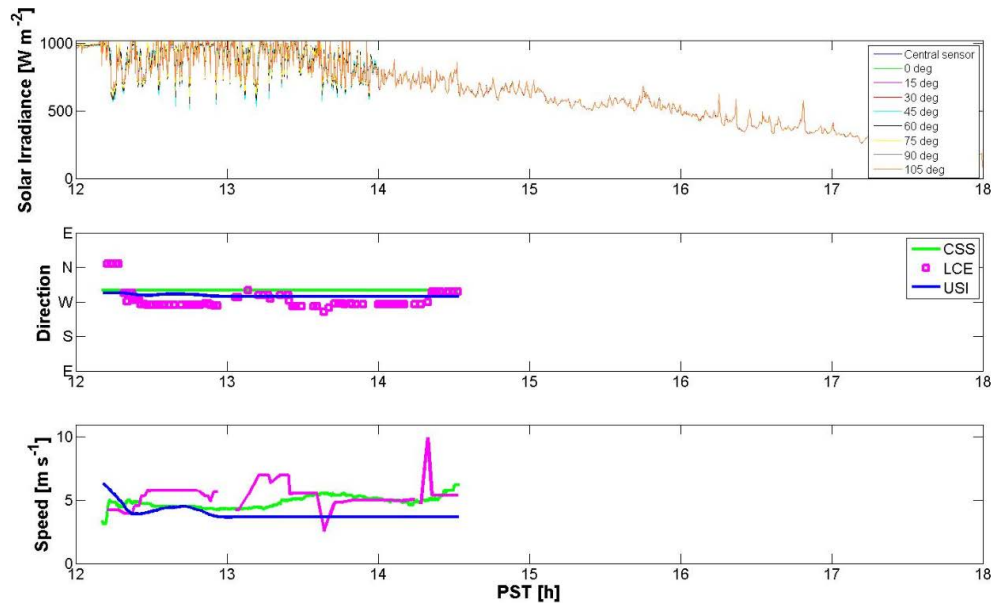
Fig. 5. Solar irradiance and cloud motion vector for the cloud speed sensor deployment on 23 July compared to USI and LCE results. Luminance measurements were calibrated against the central sensor which in turn was calibrated against a nearby pyranometer to obtain $W\,m^{-2}$ of solar irradiance.
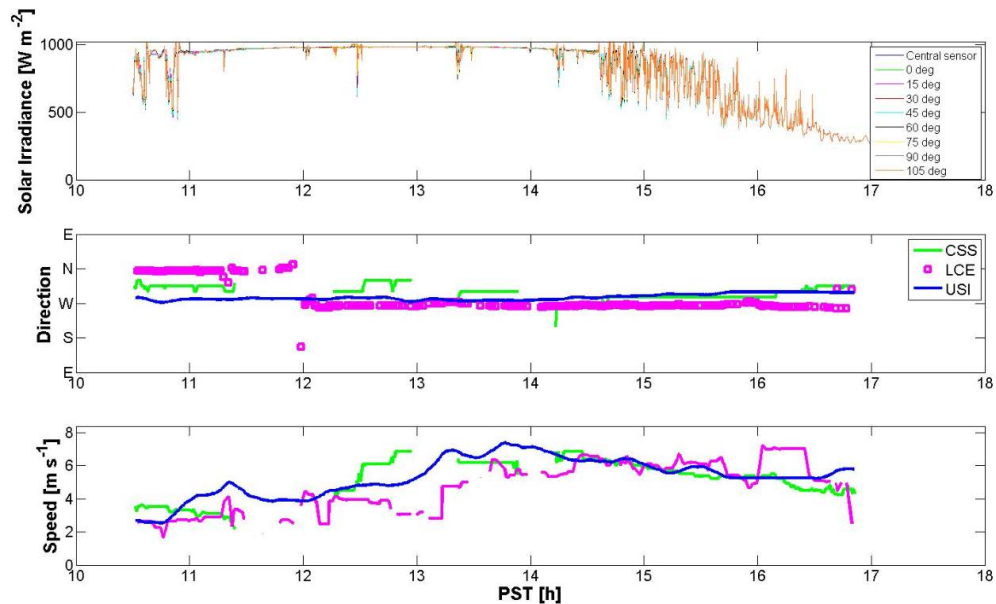
Fig. 6. Solar irradiance and cloud motion vector detected during the CSS deployment on 8 August 2013.